Communication

Effect of the Ni-to-CaO Ratio on Integrated CO$_2$ Capture and Direct Methanation

Jin-Hyeok Woo [1],[†], Seongbin Jo [2],[†], Ju-Eon Kim [1], Tae-Young Kim [3], Han-Dong Son [1], Ho-Jung Ryu [4], Byungwook Hwang [4], Jae-Chang Kim [1],[*], Soo-Chool Lee [3],[*] and Kandis Leslie Gilliard-AbdulAziz [2],[5],[*]

[1] Department of Chemical Engineering, Kyungpook National University, Daegu 41566, Republic of Korea; wjh8865@knu.ac.kr (J.-H.W.); lawliet@knu.ac.kr (J.-E.K.); coma133he@knu.ac.kr (H.-D.S.)
[2] Department of Chemical and Environmental Engineering, University of California–Riverside, Riverside, CA 92521, USA; sjo016@ucr.edu
[3] Research Institute of Advanced Energy Technology, Kyungpook National University, Daegu 41566, Republic of Korea; tyoung0218@knu.ac.kr
[4] Korea Institute of Energy Research, Daejeon 34129, Republic of Korea; hjryu@kier.re.kr (H.-J.R.); hbw@kier.re.kr (B.H.)
[5] Department of Material Science and Engineering, University of California–Riverside, Riverside, CA 92521, USA
[*] Correspondence: kjchang@knu.ac.kr (J.-C.K.); soochool@knu.ac.kr (S.-C.L.); klabulaziz@engr.ucr.edu (K.L.G.-A.)
[†] These authors contributed equally to this work.

Abstract: Direct methanation in an integrated CO$_2$ capture and utilization system has recently gained considerable attention as a promising approach owing to its simplified process and lower requirement of total thermal energy as compared to conventional CO$_2$ capture and utilization techniques. This study formulated macroporous structured Ni/CaO catal-sorbents by controlling the Ni-to-CaO ratio. The influence of this ratio on the CO$_2$ capture (capacity and kinetics) and direct methanation performances (productivity and kinetics) was evaluated at 500 °C. CO$_2$ capture combined with direct methanation experiments revealed that 10Ni/CaO exhibited the best CO$_2$ capture capacity, kinetics, and CH$_4$ productivity with the thermal stability of Ni and CaO species.

Keywords: ICCU; direct methanation; Ni/CaO ratio; macroporous structure; Ni dispersion
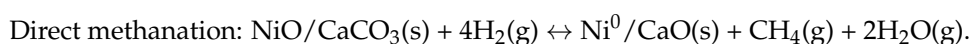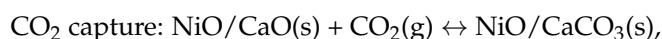
1. Introduction

Carbon dioxide (CO$_2$) emissions are an important cause of global climate change and a major challenge our planet is facing today. The burning of fossil fuels, such as coal, oil, and gas, for energy and transportation is the primary source of CO$_2$ emissions. These emissions trap heat in the atmosphere and lead to global warming, which has various adverse effects on the environment, including sea-level rise, extreme weather events, and the loss of biodiversity [1–5]. CO$_2$ capture and utilization (CCU) technology captures CO$_2$ emissions from various sources and converts them into value-added products. This technology has gained considerable attention as a means to mitigate climate change and greenhouse gas emissions. The captured CO$_2$ can be used to produce fuels, chemicals, and other products through various conversion methods, such as biological, chemical, and electrochemical processes [3,6]. By utilizing the captured CO$_2$, CCU technology not only reduces emissions but also contributes to the circular economy by producing sustainable products. In addition, CO$_2$ utilization may decrease the dependency on fossil fuels, thereby promoting a sustainable future. With continued research and development, CCU technology may become a feasible solution to the challenges of climate change while supporting economic growth [3,7].

Recently, there has been a growing interest in the integrated CO$_2$ capture and utilization (ICCU) technology that uses dual functional materials to combine CO$_2$ capture and

utilization in a single reaction system. ICCU technology is promising for mitigating climate change by reducing CO_2 emissions while producing valuable products. This technology involves capturing CO_2 from industrial processes, transport, and power plants, followed by its utilization in various green technologies [8–21]. Calcium looping technology is one of the effective methods for CO_2 capture, which employs a calcium oxide (CaO)-based solid sorbent to chemically absorb CO_2 [12,22–24]. However, the sintering-induced decrease in CO_2 capture capacity during carbonation and regeneration cycles limits the efficiency of these sorbents [23]. To improve their multicycle stability, metal oxide stabilizers are added to the intraparticle region of CaO, which increases the length of diffusional paths, decreases the sintering rate, and enhances the textural properties of these sorbents [12,22–24].

Owing to the characteristics of ICCU technology, where CO_2 capture and conversion must occur continuously in the same temperature range, only CO_2 methanation through the Sabatier reaction is suitable for intermediate temperature conversion. The methanation reaction is the simplest and the most efficient catalytic CO_2 utilization process, which converts CO_2 and H_2 to CH_4, which is an energy carrier with the least CO_2 emission per unit of energy among fossil fuels [17–20,25–27]. Direct methanation after CO_2 capture in flue gas conditions through Ni-CaO occurs as follows [28,29]:

$$CO_2 \text{ capture: } NiO/CaO(s) + CO_2(g) \leftrightarrow NiO/CaCO_3(s),$$

$$\text{Direct methanation: } NiO/CaCO_3(s) + 4H_2(g) \leftrightarrow Ni^0/CaO(s) + CH_4(g) + 2H_2O(g).$$

In our previous paper, an ICCU-direct methanation process using a 10Ni/CaO catal-sorbent was proposed, and the optimum temperature was determined to be 500 °C, considering the high CO_2 capture capacity, CH_4 selectivity, and thermal stability of the catal-sorbent [28,29]. Herein, Ni/CaO catal-sorbents with different Ni-to-CaO ratios were synthesized by the sol–gel method to determine the effect of these ratios on the macroporous of CaO and Ni dispersion. Textural structure of the Ni/CaO catal-sorbents is critically important since the pore structure enables rapid CO_2 diffusion for CO_2 capture capacity and the Ni dispersion promotes catalytic activity. Their CO_2 capture performance (capacity and kinetics) and direct methanation performance (productivity and kinetics) according to the textural structure were studied. Moreover, the cycle stability of the catal-sorbents in CO_2 capture and direct methanation was revealed. The optimal Ni/CaO ratio was proposed through CO_2 capture and direct methanation performance results and analysis.

2. Results and Discussion

2.1. Characterization

The ICP-OES metal content, BET surface area, nanoparticle size, and porosity of 2Ni/CaO, 10Ni/CaO, and 20Ni/CaO catal-sorbents are summarized in Table 1. The Ni metal contents of the 2Ni/CaO, 10Ni/CaO, and 20Ni/CaO catal-sorbents prepared by the citrate sol–gel method are 1.6, 9.3, and 18.0 wt.%, respectively, which are consistent with the desired metal loading. The BET surface area of 2Ni/CaO, 10Ni/CaO, and 20Ni/CaO catal-sorbents are 4.59, 9.90, and 7.77 m^2/g, respectively, and 10Ni/CaO has the smallest nanoparticle size of 605.8 nm. As can be seen in Figure 1, 2Ni/CaO has a dense morphology, with interconnected nanoparticle structures and poor porosity. Notably, as the Ni-to-CaO ratio increases the porous structures expand, and the nanoparticle size decreases dramatically; 2Ni/CaO, 10Ni/CaO, and 20Ni/CaO exhibited porosities 72.9, 74.7, and 74.4%, respectively. In addition, the Hg porosimeter revealed that macroporous structures > 100 nm increase as the Ni-to-CaO ratio increases (Figure S1). 10Ni/CaO exhibited exceptional BET surface area, nanoparticle size, and porosity among xNi/CaO catal-sorbents. Figure 1d–f present the TEM images and the Ni crystallite size distribution of the catal-sorbents. The energy dispersive spectroscopy (EDS) mapping on the catal-sorbents revealed that Ni nanoparticles of uniform size are dispersed uniformly throughout CaO (Figures S2–S4). Individual Ni particles in 2Ni/CaO, 10Ni/CaO, and 20Ni/CaO had an average crystallite

size of 20.2, 27.0, and 45.4 nm, respectively (Table 2). 2Ni/CaO exhibited the highest Ni dispersion (2.43%) and Ni surface area (16.19 m^2/gNi), and Ni dispersion and Ni surface area decreased with the increase in the Ni-to-CaO ratio, leading to poor catalytic activity.

Table 1. Metal contents, BET surface area, nanoparticle size, and porosity of the 2Ni/CaO, 10Ni/CaO, and 20Ni/CaO catal-sorbents in their fresh states.

	Metal Contents	BET Surface	Nanoparticle Size (nm)	Porosity
	(wt.%)	Area (m^2/g)		(%)
2Ni/CaO	Ni: 1.6 CaO: 98.4	4.59	1307	72.9
10Ni/CaO	Ni: 9.3 CaO: 90.7	9.9	605.8	74.68
20Ni/CaO	Ni: 18.0 CaO: 82.0	7.77	771.6	74.39
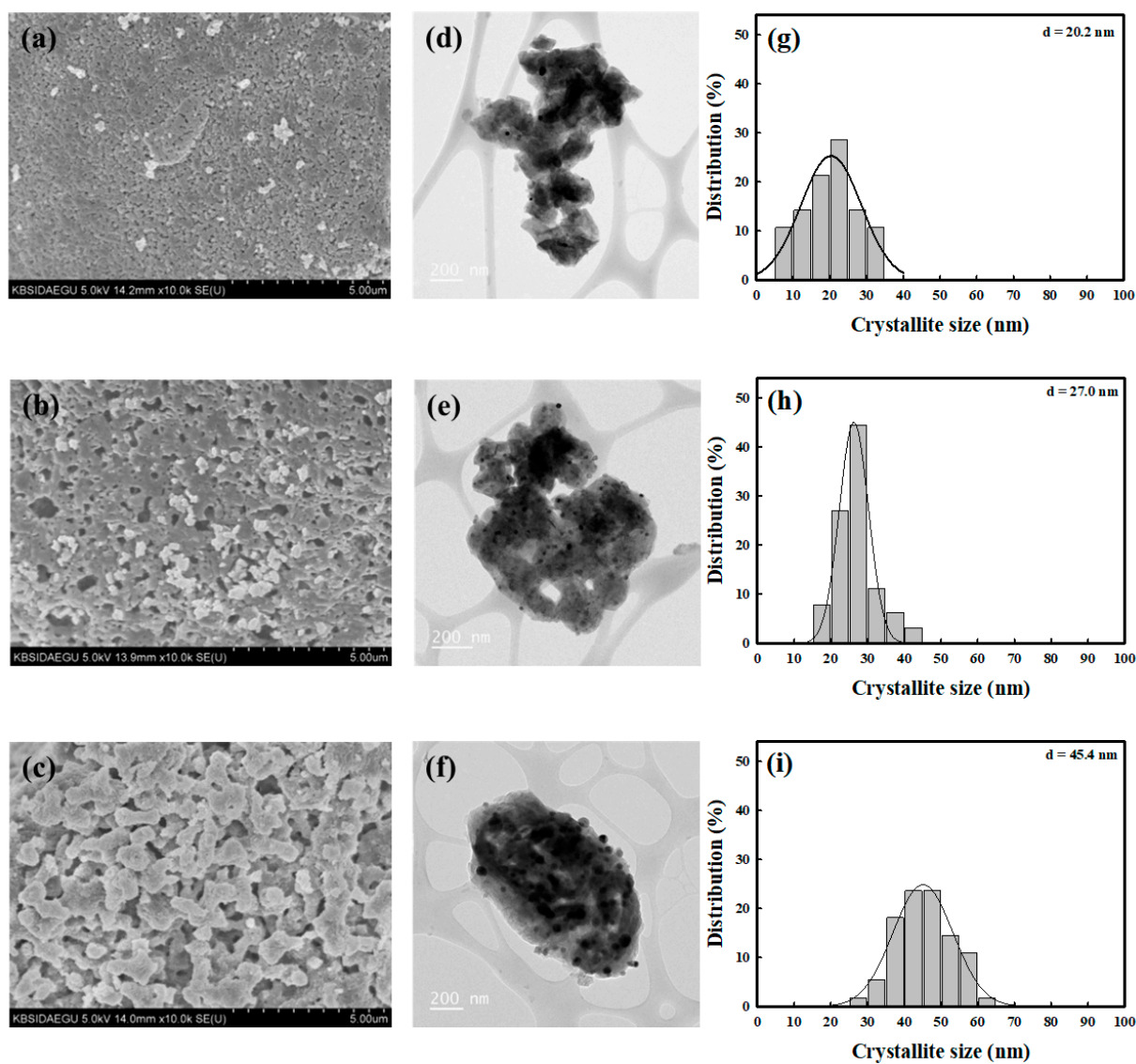
Figure 1. SEM images, TEM images, and Ni crystallite size of (**a**,**d**,**g**) 2Ni/CaO, (**b**,**e**,**h**) 10Ni/CaO, and (**c**,**f**,**i**) 20Ni/CaO catal-sorbents prepared by the citrate sol–gel method.

Table 2. Ni crystallite size, Ni dispersion, and Ni surface area of the 2Ni/CaO, 10Ni/CaO, and 20Ni/CaO catal-sorbents.

	Ni Crystallite Size [a] (nm)	Dispersion [b] (%)	Ni surface Area [b] (m^2/g_{Ni})
2Ni/CaO	20.2	2.43	16.19
10Ni/CaO	27.0	0.11	0.72
20Ni/CaO	45.4	0.09	0.58

[a] Measured by TEM. [b] Calculated from CO chemisorption.

In Figure 2a, the XRD patterns of 2Ni/CaO, 10Ni/CaO, and 20Ni/CaO in the fresh state display NiO (JCPDS No. 89-7131) and CaO phase (JCPDS No. 48-1467). In addition to the NiO phase, a very small and broad peak of metallic Ni is observed for 20Ni/CaO. 2Ni/CaO, 10Ni/CaO, and 20Ni/CaO have CaO crystallite sizes of 49.7, 50.1, and 32.2 nm, respectively. The crystallite size of CaO decreased with increasing Ni-to-CaO ratio, and the smallest CaO in 20Ni/CaO is expected to be the fastest kinetics in CO_2 capture. In Figure 2b, the XPS spectra of Ni $2p_{3/2}$ revealed that Ni^{2+} exists in two states within the catal-sorbents. The peak with the lowest binding energy (853.5–854.5 eV) corresponds to the bulk NiO (Ni^{2+} (I)), whereas the peak with a higher binding energy (855.5–856 eV) is attributed to the NiO interacting with CaO (Ni^{2+} (II)) [29–31]. The intensity ratio of Ni^{2+} (I) and Ni^{2+} (II) increased as the Ni concentration increased from 2 to 20 wt.%. This is because for catal-sorbents with larger Ni crystallite sizes (e.g., 20Ni/CaO), there may be a greater increase in the amount of bulk NiO relative to the amount of NiO interacting with CaO. In the XRD results, very small peaks of Ni^0 were observed for 20Ni/CaO. The H_2-TPR profiles of Ni/CaO catal-sorbents (Figure S5) revealed that NiO phases can be converted to metallic Ni under direct methanation conditions. The H_2-TPR curves for 2Ni/CaO, 10Ni/CaO, and 20Ni/CaO exhibit two groups of peaks at maximum temperatures of ~380 °C and 450–500 °C. The lower temperature event is attributed to the bulk reduction of NiO, indicating minimal or no interaction with the CaO phase, whereas the higher temperature event corresponds to NiO interacting strongly with CaO [31].
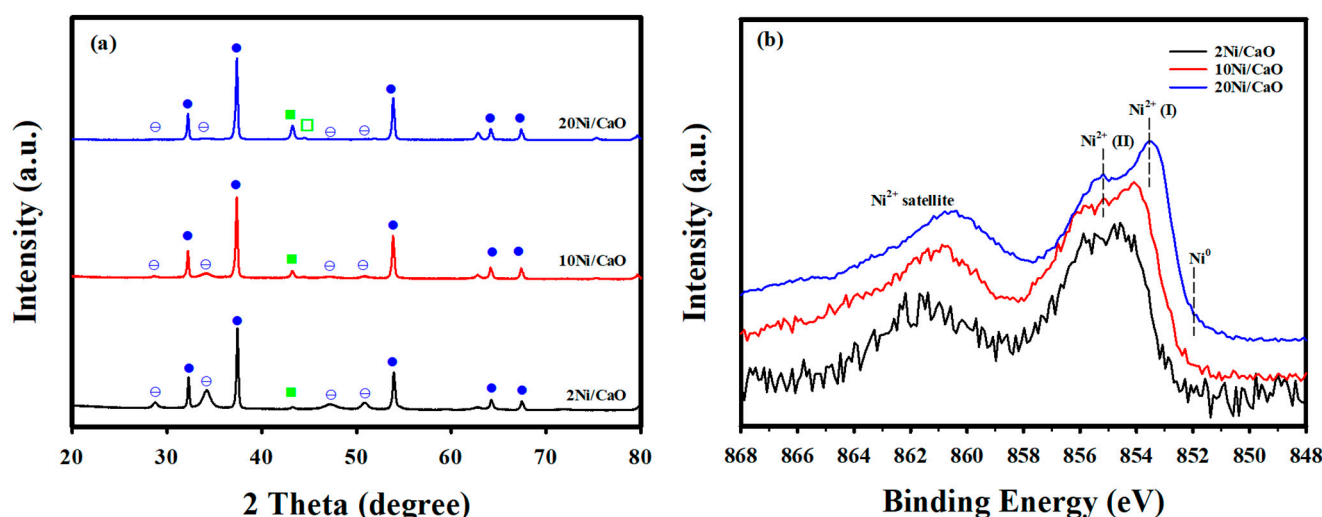

Figure 2. (**a**) XRD patterns of 2Ni/CaO, 10Ni/CaO, and 20Ni/CaO catal-sorbents in fresh states: (■) NiO and (□) Ni0, (●) CaO and (⊖) Ca(OH)$_2$. (**b**) XPS spectra of Ni $2p_{3/2}$ in the 2Ni/CaO, 10Ni/CaO, and 20Ni/CaO catal-sorbents.

2.2. Evaluation of Catal-Sorbent Performance

CO_2 capture and direct methanation in the ICCU process during five cycles under 10 vol.% CO_2 and 10 vol.% H_2O at 500 °C using the catal-sorbents and the corresponding profiles are depicted in Figure 3. The breakthrough curves of 2Ni/CaO, 10Ni/CaO, and 20Ni/CaO are shown in Figure 3a. The breakthrough time slightly increased with increasing Ni-to-CaO ratio because of the enhanced macroporous structures and the smaller size of CaO, despite the decrease in CaO amount. In the initial cycle, the total CO_2 capture capacities of 2Ni/CaO, 10Ni/CaO, and 20Ni/CaO, which were calculated from the breakthrough curves, were 5.89, 8.96, and 9.87 mmol CO_2/g catal-sorbent, respectively (Table 3). 20Ni/CaO showed the highest CO_2 capture capacity owing to the smallest crystallite size of CaO and improved macroporous structure. Figure 3b shows the CH_4 concentration for 2Ni/CaO, 10Ni/CaO, and 20Ni/CaO during direct methanation. Further, it was observed that the maximum CH_4 concentration in the direct methanation step decreased with increasing Ni-to-CaO ratio. However, 20Ni/CaO exhibited the highest CH_4 productivity at the initial cycle as it has the highest CO_2 capture capacity, and all CO_2 was converted to CH_4 (i.e., 100% CH_4 selectivity) during direct methanation (Table 3).
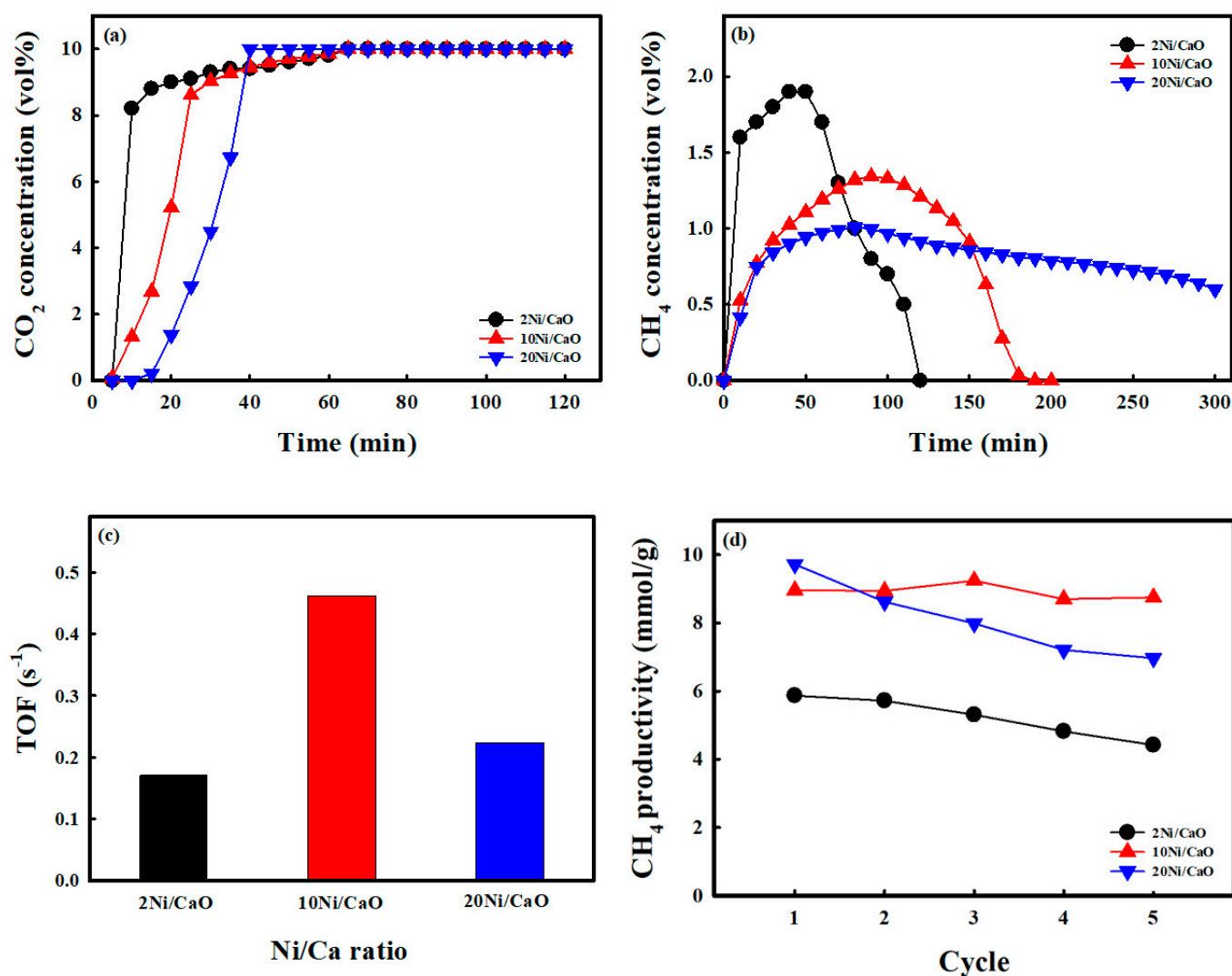

Figure 3. CO_2 capture and direct methanation capacity and behavior of 2Ni/CaO, 10Ni/CaO, and 20Ni/CaO catal−sorbents (**a,b**) in the initial cycle, (**c**) apparent TOF of 2Ni/CaO, 10Ni/CaO, and 20Ni/CaO catal-sorbents in the initial cycle, and (**d**) over five consecutive cycles. (CO_2 capture: 10 vol.% CO_2 and 10 vol.% H_2O; direct methanation: 90 vol.% H_2 at 500 °C).

Table 3. CO_2 capture and direct methanation performances of the 2Ni/CaO, 10Ni/CaO, and 20Ni/CaO catal-sorbents over five consecutive cycles at 500 °C.

		CO$_2$ Capture	Direct Methanation		
	Cycle	CO$_2$ Captured (mmol/g)	CH$_4$ Produced (mmol/g)	CH$_4$ Selectivity (%)	Carbon Balance (%)
2Ni/CaO	1	5.89	5.88	100	99.8
	2	5.75	5.75	100	100
	3	5.33	5.33	100	100
	4	4.84	4.83	100	99.8
	5	4.45	4.44	100	100
10Ni/CaO	1	8.96	8.95	100	99.9
	2	8.94	8.93	100	99.9
	3	9.24	9.24	100	100
	4	8.70	8.70	100	100
	5	8.75	8.75	100	100
20Ni/CaO	1	9.87	9.72	100	98.5
	2	8.70	8.62	100	99.1
	3	8.16	7.98	100	97.8
	4	7.39	7.21	100	97.6
	5	7.15	6.97	100	97.5

The catalytic activity of the catal-sorbents in the direct methanation step was quantified by calculating the apparent turnover frequency (TOF), as shown below [32]:

$$\text{TOF (s}^{-1}) = \frac{r_{CH_4} \cdot M}{W \cdot D \cdot x} \tag{1}$$

where r_{CH_4} denotes the CH_4 production rate during direct methanation (mol/s), M is the atomic mass of Ni (g/mol), W indicates the weight of the catalyst packed into the reactor (g), D denotes the dispersion of Ni particles on the surface of the catalyst, and x denotes the loading weight ratio of Ni in the catalyst. Figure 3c shows the apparent TOF of the catal-sorbents obtained at the highest CH_4 concentration during direct methanation in the initial cycle. The TOF increased from 0.1707 s^{-1} for 2Ni/CaO to 0.4621 s^{-1} for 10Ni/CaO and then decreased to 0.2232 s^{-1} for 20Ni/CaO. Figure 3d shows the CH_4 productivity over five cycles of ICCU methanation steps for the catal-sorbents. The CO_2 capture capacities of 2Ni/CaO and 20Ni/CaO catal-sorbents decreased gradually over multiple cycles, resulting in a gradual decline in CH_4 productivity at the subsequent direct methanation step (Figure S6). Further, it was observed that the breakthrough time of 2Ni/CaO slightly decreased as the cycle test progressed. Nevertheless, the kinetics of direct methanation in 2Ni/CaO were stable throughout the cycles. In contrast to 2Ni/CaO, the breakthrough time of 20Ni/CaO was stable. However, the CO_2 capture capacity decreased in subsequent reaction cycles because of the incomplete regeneration of $CaCO_3$ by slow direct methanation. 20Ni/CaO exhibited a relatively sluggish direct methanation rate, and the rate was decreasing as the number of reaction cycles increased, leading to a decrease in CH_4 productivity from 9.72 to 6.97 mmol CH_4/g catal-sorbent. 10Ni/CaO exhibited excellent thermal stability with high CH_4 productivity (8.95–8.75 mmol CH_4/g catal-sorbent) over five cycles of ICCU methanation because of its high CO_2 capture capacity, fast carbonation, and direct methanation by the improved macroporous CaO structure and Ni dispersion. The CaO phase in the catal-sorbents is converted to $CaCO_3$ by CO_2 absorption after the first carbonation at 500 °C for 2 h, and the CaO conversion ratio increases with increasing Ni-to-CaO ratio (Figure 4a), corresponding to the CO_2 capture performance presented in Figure 3a. As shown in Figure 1b, NiO is reduced to Ni, and $CaCO_3$ is regenerated to CaO/Ca(OH)$_2$ phases during direct methanation. However, for 20Ni/CaO, not all $CaCO_3$ is regenerated after the fifth direct methanation because of the slow methanation rate, as mentioned above. After the sixth CO_2 capture, the Ni phase is

converted back to the NiO phase by the oxidation of metallic Ni by CO_2 or H_2O in the CO_2 capture step [28,29]. It is observed that the CaO conversion ratio in 2Ni/CaO decreased, compared to the first CO_2 capture. This might be because 2Ni/CaO has the largest CaO crystallite size and the poorest macroporous structures among the catal-sorbents, and CO_2 cannot diffuse through the thick layer of $CaCO_3$ to come in contact with the inner CaO phase. For 10Ni/CaO, the conversion of CaO to $CaCO_3$ increased, which may be due to the redispersion of the CaO phase. However, for 20Ni/CaO, the increase in CaO conversion after the sixth CO_2 capture is caused by incomplete decarbonation during direct methanation.
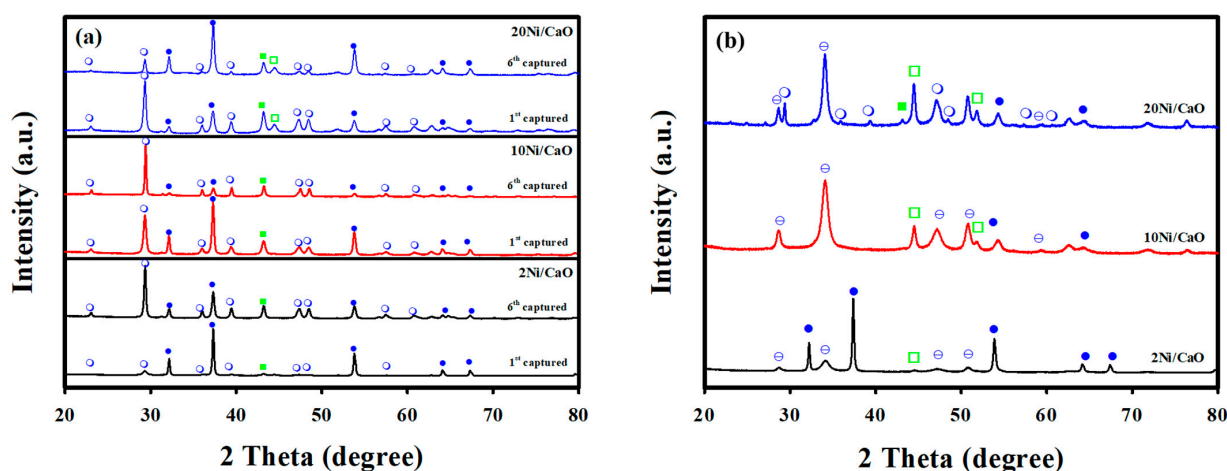

Figure 4. XRD patterns of 2Ni/CaO, 10Ni/CaO, and 20Ni/CaO catal-sorbents after (**a**) the first and sixth CO_2 capture, and (**b**) fifth direct methanation in the ICCU process: (■) NiO and (□) Ni0, (●) CaO and (⊖) $Ca(OH)_2$, and (○) $CaCO_3$.

After five consecutive cycles of CO_2 capture and direct methanation, the crystallite size of Ni species in 2Ni/CaO and 10Ni/CaO increased slightly from 20.2 and 26.9 to 32.3 and 37.8 nm, respectively (Figure 5). Despite the increase in the crystallite size of Ni in 2Ni/CaO and 10Ni/CaO catal-sorbents, the kinetics of direct methanation maintained stability because of the relatively high Ni dispersion. 20Ni/CaO shows high bulk NiO (Ni^{2+} (I)) in the XPS results, which explains the large Ni particle size. The large size of the Ni particles means that the dispersion of Ni is low. This exhibited a sluggish direct methanation rate (Figure S6). 20Ni/CaO has a higher amount of bulk NiO compared to the amount of NiO interacting with CaO (Ni^{2+} (II)) due to the large particle size of Ni. Many bulk NiO produced rapid sintering of Ni species after five consecutive cycles in CO_2 capture and direct methanation (Figure 5f). The increase in the Ni crystallite size correlates with the gradual deactivation of CH_4 productivity as the cycle progresses.
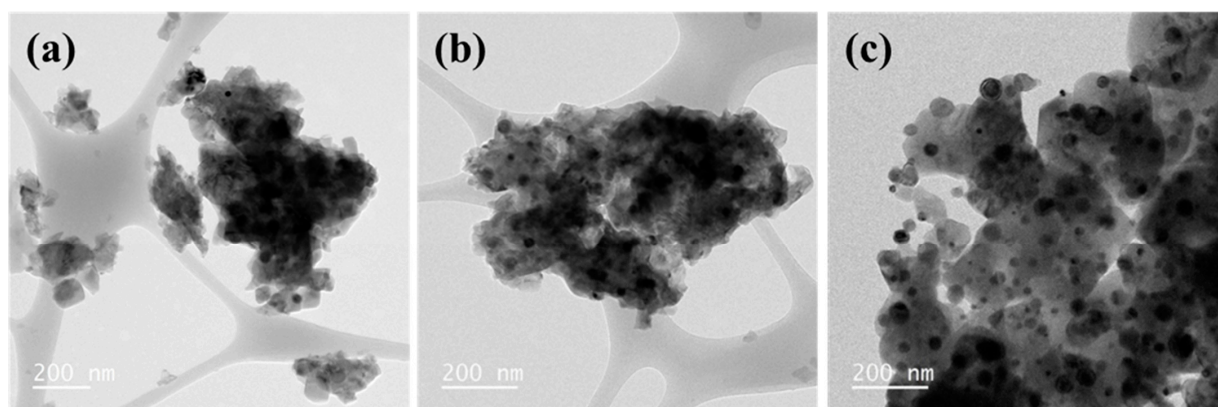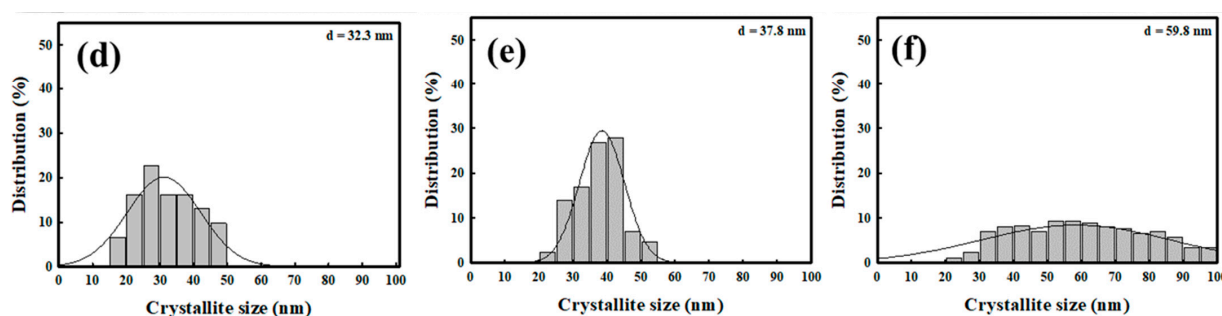

Figure 5. *Cont.*

Figure 5. TEM images and Ni crystallite size of (**a**,**d**) 2Ni/CaO, (**b**,**e**) 10Ni/CaO, and (**c**,**f**) 20Ni/CaO catal-sorbents after five cycles in CO_2 capture and direct methanation in the ICCU process.

3. Materials and Methods

3.1. Catal-Sorbent Synthesis

Nickel (II) nitrate hexahydrate ($Ni(NO_3)_2 \cdot 6H_2O$) and calcium nitrate tetrahydrate ($Ca(NO_3)_2 \cdot 4H_2O$) were used as Ni and Ca precursors, respectively, and citric acid was used as a chelating agent. The 2Ni/CaO, 10Ni/CaO, and 20Ni/CaO catal-sorbents were prepared by citrate sol–gel techniques [28,29]. Metal precursors and citric acid were dissolved in deionized water, and the solution was vigorously stirred at 50 °C for 1 h. Then, the solution was dried overnight in an oven at 100 °C to obtain a gel. The resulting dry gel was finely ground and calcined in a furnace at 800 °C for 5 h (temperature ramp rate of 10 °C/min). The resulting catal-sorbents were designated as xNi/CaO, where x represents the weight percentage of the metallic Ni based on the catal-sorbents.

3.2. Catal-Sorbent Characterization

The metal contents (Ni and Ca) of the catal-sorbents were determined using inductively coupled plasma–optical emission spectrometry (ICP-OES, OPTIMA 4300 DV, PerkinElmer, Waltham, MA, USA). Textural properties such as the Brunauer, Emmett, and Teller (BET) surface area, pore volume, average pore size, and nanoparticle size were estimated from the N_2 adsorption–desorption isotherms at −196 °C using Micromeritics ASAP 2020 (Norcross, GA, USA) analyzer. The Ni dispersion and surface area were determined by a CO chemisorption experiment using a Micromeritics ASAP 2020 analyzer. The average pore size was calculated by the Barrett–Joyner–Halenda method, and macroporosity and pore size distribution were measured by a Hg porosimeter (AutoPore V 9620, Micromeritics, Norcross, GA, USA). The morphology of the catal-sorbents was determined through field emission scanning electron microscopy (FE-SEM, S-4800, Hitachi, Tokyo, Japan), and the crystalline phase was determined through field emission transmission electron microscopy (FE-TEM, JEM-2100F, JEOL, Tokyo, Japan). The chemical composition of the surface of the catal-sorbents was obtained using an X-ray photoelectron spectrometer (XPS) using a NEXSA (ThermoFisher, Waltham, MA, USA) equipped with an Al Kα source. Differential thermal gravity curves on an SDT Q600 thermogravimetric analyzer were used to evaluate the reduction properties. The crystallographic structure of the catal-sorbents was determined by X-ray diffraction (XRD) analysis (Phillips X′PERT X-ray diffractometer, PANalytical, Amsterdam, Netherlands) using a Cu Kα radiation source. The crystallite size of CaO in the catal-sorbents was calculated by the Scherrer equation. In addition, thermogravimetric analysis (TGA, N-1000, Scinco, Seoul, Korea) was utilized to assess the cyclic regeneration properties of the catal-sorbents during CO_2 capture and direct methanation (CO_2 capture: pure CO_2 and direct methanation: pure H_2 at 500 °C).

3.3. Reaction Process

The CO_2 capture and direct methanation in the ICCU process was carried out using 0.5 g of catal-sorbents in a packed-bed reactor (inner diameter of $\frac{1}{2}$ inch). The reactor was placed in an electric furnace at atmospheric pressure. The reaction temperatures during CO_2 capture and direct methanation were maintained at 500 °C. At the CO_2 capture step,

10 vol.% CO_2, 10 vol.% H_2O, and balance N_2 were made to flow through the packed bed with 40 mL/min of total flow rate. At the direct methanation step, 90 vol.% H_2 and balance N_2 were passed after purging the reactor. N_2 was used as the balancing and standard gas. The outlet gases were analyzed through gas chromatography (GC, Agilent 6890, Agilent Technologies, Santa Clara, CA, USA) equipped with two thermal conductivity detectors (TCD). A Porapak Q packed column was used to separate N_2, CO_2, and H_2O during CO_2 capture, whereas a Carboxen-1000 packed column was used to separate H_2, N_2, CH_4, and CO_2 during direct methanation step.

4. Conclusions

Herein, Ni/CaO catal-sorbents were prepared by the sol–gel method to determine the effect of the Ni-to-CaO ratio on CO_2 capture and direct methanation performances. With increasing Ni-to-CaO ratio, the macroporous structures and crystallite size of Ni species increased, whereas the extent of nanoparticle agglomeration and the crystallite size of CaO decreased. The CO_2 capture breakthrough time slightly increased with increasing Ni-to-CaO ratio because of the enhanced macroporous structures and the smaller size of CaO. In the direct methanation step, 20Ni/CaO showed the lowest methane production due to the large Ni particle size. 10Ni/CaO showed the best TOF results (0.4621 s^{-1}) in the initial cycle with appropriate Ni dispersion and macroporous structure. The CO_2 capture and CH_4 production performances (capacity and kinetics) in 2Ni/CaO and 20Ni/CaO catal-sorbents decreased gradually over five consecutive cycles. After five consecutive cycles of CO_2 capture and direct methanation, despite the increase in the crystallite size of Ni species in 2Ni/CaO and 10Ni/CaO catal-sorbents, the kinetics of direct methanation maintained stability because of the relatively high Ni dispersion. 10Ni/CaO exhibited excellent thermal stability with high CH_4 productivity over five cycles in ICCU methanation because of its high CO_2 capture capacity, fast carbonation, and direct methanation by the improved macroporous CaO structure and Ni dispersion. Overall, the 10Ni/CaO catal-sorbent showed promise for cost-effective CO_2 capture and conversion value-added products. In the future study, long-term stability tests will be conducted to study deactivation and its effect on catalyst performance.

Author Contributions: Conceptualization, J.-H.W. and S.J.; formal analysis, J.-E.K., T.-Y.K., H.-D.S., H.-J.R. and B.H.; investigation, J.-H.W., S.J., J.-E.K., T.-Y.K. and H.-D.S.; supervision, S.-C.L., J.-C.K. and K.L.G.-A.; writing—original draft, J.-H.W. and S.J.; writing—review and editing, J.-H.W. and S.-C.L. All authors have read and agreed to the published version of the manuscript.

Data Availability Statement: The data presented in this study are available on request from the corresponding author. Data are contained within the article or Supplementary Material.

Conflicts of Interest: The authors declare no conflict of interest.

References

1. Guo, Z.-L.; Bian, X.-L.; Du, Y.-B.; Zhang, W.-C.; Yao, D.-D.; Yang, H.-P. Recent advances in integrated carbon dioxide capture and methanation technology. *J. Fuel Chem. Technol.* **2023**, *51*, 293–302. [CrossRef]
2. Yang, N.; Kang, F.; Liu, Z.; Ge, X.; Zhou, Y. An integrated CCU-plant scheme and assessment for conversion of captured CO_2 into methanol. *Int. J. Low-Carbon Technol.* **2022**, *17*, 550–562. [CrossRef]

3. Ho, H.-J.; Iizuka, A.; Shibata, E. Carbon capture and utilization technology without carbon dioxide purification and pressurization: A review on its necessity and available technologies. *Ind. Eng. Chem. Res.* **2019**, *58*, 8941–8954. [CrossRef]

4. Fernández, J.; Sotenko, M.; Derevschikov, V.; Lysikov, A.; Rebrov, E.V. A radiofrequency heated reactor system for post-combustion carbon capture. *Chem. Eng. Process.* **2016**, *108*, 17–26. [CrossRef]

5. Chronopoulos, T.; Fernandez-Diez, Y.; Maroto-Valer, M.M.; Ocone, R.; Reay, D.A. CO_2 desorption via microwave heating for post-combustion carbon capture. *Microporous Mesoporous Mat.* **2014**, *197*, 288–290. [CrossRef]

6. Varvoutis, G.; Lykaki, M.; Stefa, S.; Binas, V.; Marnellos, G.E.; Konsolakis, M. Deciphering the role of Ni particle size and nickel-ceria interfacial perimeter in the low-temperature CO_2 methanation reaction over remarkably active Ni/CeO_2 nanorods. *Appl. Catal. B-Environ.* **2021**, *297*, 120401. [CrossRef]

7. Rezaei Sadr, N.; Bahrdo, T.; Taghizadeh, R. Impacts of Paris agreement, fossil fuel consumption, and net energy imports on CO_2 emissions: A panel data approach for three West European countries. Clean Technol. *Environ. Policy* **2022**, *24*, 1521–1534. [CrossRef]

8. Wang, G.; Guo, Y.; Yu, J.; Liu, F.; Sun, J.; Wang, X.; Wang, T.; Zhao, C. Ni-CaO dual function materials prepared by different synthetic modes for integrated CO_2 capture and conversion. *Chem. Eng. J.* **2022**, *428*, 132110. [CrossRef]

9. Chen, J.; Xu, Y.; Liao, P.; Wang, H.; Zhou, H. Recent progress in integrated CO_2 capture and conversion process using dual function materials: A state-of-the-art review. *Carbon Capture Sci. Technol.* **2022**, *4*, 100052. [CrossRef]

10. Zhao, Y.; Li, Y.; Jin, B.; Liang, Z. Layered double hydroxide derived bifunctional Ca-Fe-Mg material for integrated CO_2 capture and utilization via chemical looping strategy. *Chem. Eng. J.* **2022**, *431*, 133826. [CrossRef]

11. Al-Mamoori, A.; Lawson, S.; Rownaghi, A.A.; Rezaei, F. Oxidative dehydrogenation of ethane to ethylene in an integrated CO_2 capture-utilization process. *Appl. Catal. B-Environ.* **2020**, *278*, 119329. [CrossRef]

12. Lawson, S.; Baamran, K.; Newport, K.; Alghamadi, T.; Jacobs, G.; Rezaei, F.; Rownaghi, A.A. Integrated direct air capture and oxidative dehydrogenation of propane with CO_2 at isothermal conditions. *Appl. Catal. B-Environ.* **2022**, *303*, 120907. [CrossRef]

13. Sasayama, T.; Kosaka, F.; Liu, Y.; Yamaguchi, T.; Chen, S.-Y.; Mochizuki, T.; Urakawa, A.; Kuramoto, K. Integrated CO_2 capture and selective conversion to syngas using transition-metal-free $Na/Al2O3$ dual-function material. *J. CO_2 Util.* **2022**, *60*, 102049. [CrossRef]

14. Sun, S.; Sun, H.; Guan, S.; Xu, S.; Wu, C. Integrated CO_2 capture and methanation on Ru/CeO_2-MgO combined materials: Morphology effect from CeO_2 support. *Fuel* **2022**, *317*, 123420. [CrossRef]

15. Gu, H.; Gao, Y.; Iftikhar, S.; Li, F. Ce stabilized Ni–SrO as a catalytic phase transition sorbent for integrated CO_2 capture and CH_4 reforming. *J. Mater. Chem. A* **2022**, *10*, 3077–3085. [CrossRef]

16. Guo, Y.; Wang, G.; Yu, J.; Huang, P.; Sun, J.; Wang, R.; Wang, T.; Zhao, C. Tailoring the performance of Ni-CaO dual function materials for integrated CO_2 capture and conversion by doping transition metal oxides. *Sep. Purif. Technol.* **2023**, *305*, 122455. [CrossRef]

17. Sun, Z.; Shao, B.; Zhang, Y.; Gao, Z.; Wang, M.; Liu, H.; Hu, J. Integrated CO_2 capture and methanation from the intermediate-temperature flue gas on dual functional hybrids of AMS/CaMgO∥NixCoy. *Sep. Purif. Technol.* **2023**, *307*, 122680. [CrossRef]

18. Jo, S.; Cruz, L.; Shah, S.; Wasantwisut, S.; Phan, A.; Gilliard-AbdulAziz, K.L. Perspective on Sorption Enhanced Bifunctional Catalysts to Produce Hydrocarbons. *ACS Catal.* **2022**, *12*, 7486–7510. [CrossRef]

19. Jo, S.; Son, H.D.; Kim, T.-Y.; Woo, J.H.; Kim, J.C.; Lee, S.C.; Gilliard-AbdulAziz, K.L. Ru/K_2CO_3–MgO catalytic sorbent for integrated CO_2 capture and methanation at low temperatures. *Chem. Eng. J.* **2023**, *469*, 143772. [CrossRef]

20. Jo, S.; Lee, J.H.; Kim, T.Y.; Woo, J.H.; Ryu, H.-J.; Hwang, B.; Lee, S.C.; Kim, J.C.; Gilliard-AbdulAziz, K.L. A fundamental study of CO_2 capture and CH_4 production in a rapid cyclic system using nickel-lithium-silicate as a catal-sorbent. *Fuel* **2022**, *311*, 122602. [CrossRef]

21. Jo, S.; Lee, J.H.; Woo, J.H.; Kim, T.-Y.; Ryu, H.-J.; Hwang, B.; Kim, J.C.; Lee, S.C.; Gilliard-AbdulAziz, K.L. Coke-promoted Ni/CaO catal-sorbents in the production of cyclic CO and syngas. *Sustain. Energ. Fuels* **2022**, *6*, 81–88. [CrossRef]

22. Wei, S.; Han, R.; Su, Y.; Gao, J.; Zhao, G.; Qin, Y. Pore structure modified CaO-based sorbents with different sized templates for CO_2 capture. *Energy Fuels* **2019**, *33*, 5398–5407. [CrossRef]

23. Yoon, H.J.; Lee, K.B. Introduction of chemically bonded zirconium oxide in CaO-based high-temperature CO_2 sorbents for enhanced cyclic sorption. *Chem. Eng. J.* **2019**, *355*, 850–857. [CrossRef]

24. Zhang, C.; Li, Y.; He, Z.; Zhao, J.; Wang, D. Microtubular Fe/Mn-promoted CaO-$Ca_{12}Al_{14}O_{33}$ bi-functional material for H_2 production from sorption enhanced water gas shift. *Appl. Catal. B-Environ.* **2022**, *314*, 121474. [CrossRef]

25. Frontera, P.; Macario, A.; Ferraro, M.; Antonucci, P. Supported catalysts for CO_2 methanation: A review. *Catalysts* **2017**, *7*, 59. [CrossRef]

26. Tsiotsias, A.I.; Charisiou, N.D.; Yentekakis, I.V.; Goula, M.A. The role of alkali and alkaline earth metals in the CO_2 methanation reaction and the combined capture and methanation of CO_2. *Catalysts* **2020**, *10*, 812. [CrossRef]

27. Wang, S.; Schrunk, E.T.; Mahajan, H.; Farrauto, R.J. The role of ruthenium in CO_2 capture and catalytic conversion to fuel by dual function materials (DFM). *Catalysts* **2017**, *7*, 88. [CrossRef]

28. Jo, S.B.; Woo, J.H.; Lee, J.H.; Kim, T.Y.; Kang, H.I.; Lee, S.C.; Kim, J.C. CO_2 green technologies in CO_2 capture and direct utilization processes: Methanation, reverse water-gas shift, and dry reforming of methane. *Sustain. Energ. Fuels* **2020**, *4*, 5543–5549. [CrossRef]

29. Jo, S.B.; Woo, J.H.; Lee, J.H.; Kim, T.Y.; Kang, H.I.; Lee, S.C.; Kim, J.C. A novel integrated CO_2 capture and direct methanation process using Ni/CaO catal-sorbents. Sustain. *Energ. Fuels* **2020**, *4*, 4679–4687.

30. Hu, J.; Hongmanorom, P.; Galvita, V.V.; Li, Z.; Kawi, S. Bifunctional Ni-Ca based material for integrated CO_2 capture and conversion via calcium-looping dry reforming. *Appl. Catal. B-Environ.* **2021**, *284*, 119734. [CrossRef]

31. Tian, S.; Yan, F.; Zhang, Z.; Jiang, J. Calcium-looping reforming of methane realizes in situ CO_2 utilization with improved energy efficiency. *Sci. Adv.* **2019**, *5*, eaav5077. [CrossRef] [PubMed]

32. Lim, H.S.; Kim, G.; Kim, Y.; Lee, M.; Kang, D.; Lee, H.; Lee, J.W. Ni-exsolved La1-xCaxNiO3 perovskites for improving CO_2 methanation. *Chem. Eng. J.* **2021**, *412*, 127557. [CrossRef]